ELSEVIER

Volume 181, Number 10, October 2008

JOURNAL OF SOLID STATE CHEMISTRY

www.elsevier.com/locate/jssc

CONTENTS

Abstracted/indexed in BioEngineering Abstracts, Chemical Abstracts, Coal Abstracts, Current Contents/Physics, Chemical, & Earth Sciences, Engineering Index, Research Alert, SCISEARCH, Science Abstracts, and Science Citation Index. Also covered in the abstract and citation database SCOPUS®. Full text available on ScienceDirect®.

Regular Articles

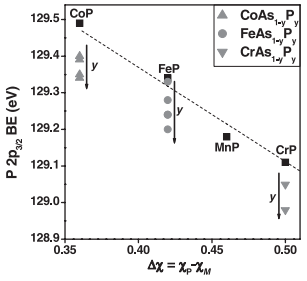

The metal arsenide phosphides $CoAs_{1-y}P_y$, $FeAs_{1-y}P_y$, and $CrAs_{1-y}P_y$ with the MnP-type structure have been studied by XPS and XANES. The shifts in the P 2*p* BEs observed for the metal arsenide phosphides compared to the binary metal phosphides cannot be explained by interaction of the nearest neighbours alone.

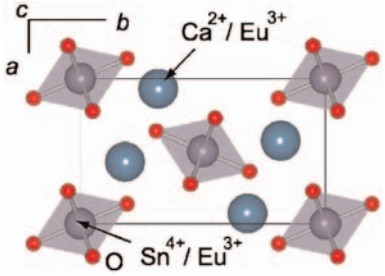

Rietveld analysis of the X-ray powder diffraction patterns revealed that Eu^{3+} replaced Ca^{2+} and Sn^{4+} in $Ca_{2-x}Eu_{2x}Sn_{1-x}O_4$, $(0 \leqslant x \leqslant 0.3)$, and Eu^{3+} replaced Ca^{2+} and Y^{3+} replaced Sn^{4+} in $Ca_{1.8}Y_{0.2}Eu_{0.2}Sn_{0.8}O_4$. Red luminescence at 616 nm due to the $^5D_o \rightarrow {}^7F_2$ transition was observed in the photoluminescence spectra of these compounds.

Regular Articles—Continued

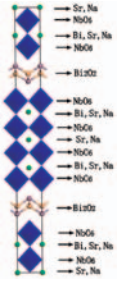

A new four-layer Aurivillius phase $Bi_2SrNa_2Nb_4O_{15}$ has been successfully synthesized. The powder X-ray diffraction shows that $Bi_2SrNa_2Nb_4O_{15}$ crystallizes in the space group *I*4/*mmm* [$a \sim 3.9021(1)$ Å, $c \sim 40.7554(10)$ Å]. Protonated form of $Bi_2SrNa_2Nb_4O_{15}$ was obtained by the substitution of bismuth oxide sheets with protons via acid treatment. The compositions of the protonated products was determined to be $H_{1.8}[Sr_{0.8}Bi_{0.2}Na_2Nb_4O_{13}]$ by X-ray fluorescence spectroscopy and thermogravimetry.

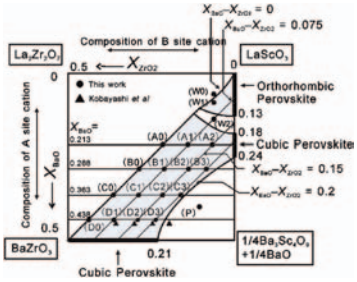

The phase boundary of solid solution between lanthanum scandate and barium zirconate at 1600 °C was clarified by establishing a partial pseudoquaternary phase diagram of the $LaO_{1.5}$–BaO–$ScO_{1.5}$–ZrO_2 system at 1600 °C.

Solid solubility and phase transitions in the system $LaNb_{1-x}Ta_xO_4$
Fride Vullum, Fabian Nitsche, Sverre Magnus Selbach and Tor Grande
Page 2580

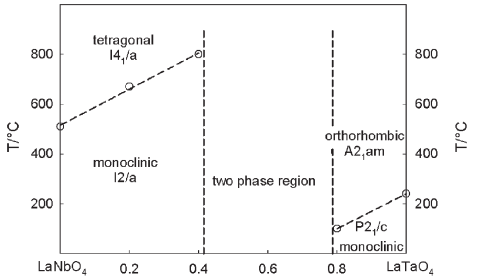

$LaNb_{1-x}Ta_xO_4$ ($0 \leqslant x \leqslant 0.4$) with the monoclinic Fergusonite structure, was observed to transform to a tetragonal Scheelite, while monoclinic $LaNb_{1-x}Ta_xO_4$ ($0.8 \leqslant x$ 1) was shown to transform to an orthorhombic crystal structure.

One-dimensional inorganic arrangement in the bismuth oxalate hydroxide $Bi(C_2O_4)OH$
Murielle Rivenet, Pascal Roussel and Francis Abraham
Page 2586

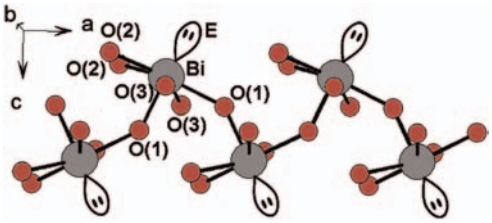

$^1_\infty[BiO_5E]$ zig-zag chains running down [100] in $Bi(C_2O_4)OH$.

The crystal structure, vibrational and luminescence properties of the nanocrystalline $KEu(WO_4)_2$ and $KGd(WO_4)_2$:Eu^{3+} obtained by the Pechini method
L. Macalik, P.E. Tomaszewski, R. Lisiecki and J. Hanuza
Page 2591

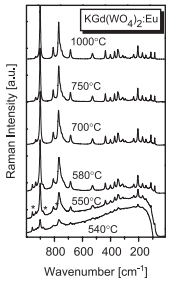

The luminescent nanocrystalline $KEu(WO_4)_2$ and $KGd_{0.98}Eu_{0.02}(WO_4)_2$ have been prepared by the Pechini method and characterise by using X-ray diffraction, infrared and Raman spectroscopy as well as optical spectroscopy. The crystal structure of $KEu(WO_4)_2$ was refined in $I2/c$ space group indicating the isostructurality to $KGd(WO_4)_2$. The size of the crystalline grains increases with the increase of the annealed temperature. The average size of crystallites of both crystals formed at 540 °C was about 50 nm. X-ray diffraction, vibrational and optical studies showed that the structure of the synthesised nanocrystalline $KEu(WO_4)_2$ and $KGd(WO_4)_2$:Eu is nearly the same as that found for the bulk material. The size-driven phase transitions were established for both compounds.

Long-range ordering in the $Bi_{1-x}Ae_xFeO_{3-x/2}$ perovskites: $Bi_{1/3}Sr_{2/3}FeO_{2.67}$ and $Bi_{1/2}Ca_{1/2}FeO_{2.75}$
C. Lepoittevin, S. Malo, N. Barrier, N. Nguyen, G. Van Tendeloo and M. Hervieu
Page 2601

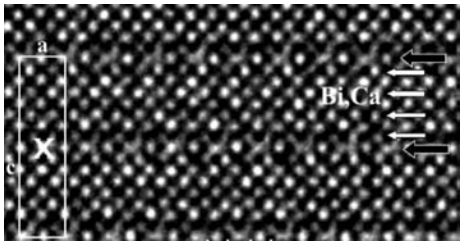

Complex long-range ordering of Bi/*Ae* cations and oxygen/vacancies consisting of 12-fold and 32-fold enlargement of the perovskite unit cell is observed in $Bi_{1/3}Sr_{2/3}FeO_{2.67}$ and $Bi_{1/2}Ca_{1/2}FeO_{2.75}$, respectively.

Layered double hydroxides as supports for intercalation and sustained release of antihypertensive drugs
Sheng-Jie Xia, Zhe-Ming Ni, Qian Xu, Bao-Xiang Hu and Jun Hu
Page 2610

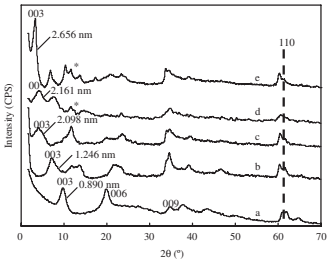

A series of antihypertensive drugs including Enalpril, Lisinopril, Captopril and Ramipril were intercalated into Zn/Al-NO_3–LDHs successfully by coprecipitation or ion-exchange technique. We focus on the structure, thermal property and low/controlled release property of as-synthesized drug–LDH composite intended for the possibility of applying these LDH–antihypertensive nanohybrids in drug delivery and controlled release systems.

Controllable preparation and properties of composite materials based on ceria nanoparticles and carbon nanotubes
Changqing Li, Nijuan Sun, Jiangfeng Ni, Jinyong Wang, Haibin Chu, Henghui Zhou, Meixian Li and Yan Li
Page 2620

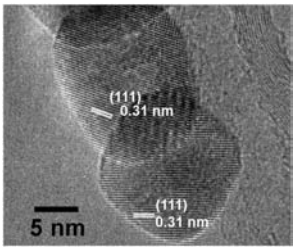

Composites based on carbon nanotubes (CNTs) and CeO_2 nanoparticles were prepared with a mild hydrothermal treatment. Larger CeO_2 nanoparticles were formed in the presence of CNTs. Grain size of CeO_2 nanoparticles in composites could be reduced when $NaNO_3$ was added. The size modulation mechanism was discussed. This CeO_2/CNTs composites could serve as promising anode materials for Li-ion batteries.

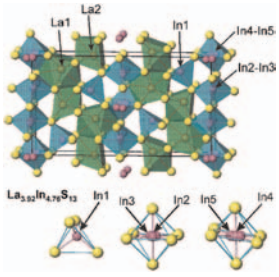

In the series of the $Ln_{4-x}In_{5-y}S_{13}$ (Ln = La, Ce, Pr and Nd; x = 0.08–0.12, y = 0.21–0.24) compounds the indium atoms occupy disordered position in the octahedral arrangement of the sulphur atoms. The tetrahedral position is ordered.

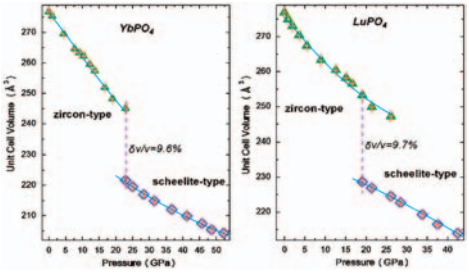

The tetragonal orthophosphates, $YbPO_4$ and $LuPO_4$, show reversible phase transitions from the zircon structure-type to the scheelite structure-type at ~22 and 19 Gpa, respectively. Coinciding with the phase transition, there is a ~10% reduction in unit cell volume.

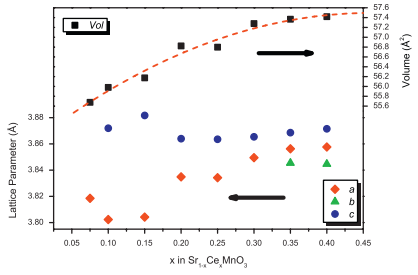

The presence of small amounts of trivalent Mn in the series $Sr_{1-x}Ce_xMnO_3$ has a dramatic effect on the structure, with the structure changing from cubic to tetragonal and finally orthorhombic. The orbital ordering present at room temperature is lost upon heating.

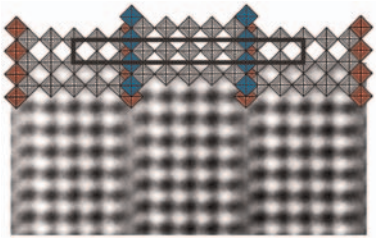

A structural model for $Al_4W_{10}O_{32}$ was derived from electron diffraction, HRTEM and HAADF-STEM observations. The ReO_3-type structure of WO_3 is sheared into five octahedra wide slabs that are connected via planes of AlO_6 octahedra. Polytypes with different slab width exist and are frequently intergrown with each other.

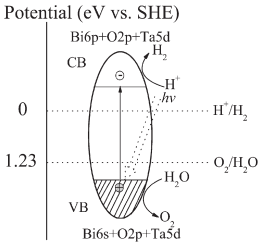

The valence band of the photocatalysts is consisted of O 2*p*, Ta 5*d* and Bi 6*s* orbitals and the conduction band is from Bi 6*p*, Ta 5*d* and O 2*p* orbitals. Photocatalytic properties of the photocatalyst for H_2 evolution without using other co-catalysts from CH_3OH/H_2O solution and O_2 evolution from $AgNO_3/H_2O$ solution were observed under Hg lamp irradiation.

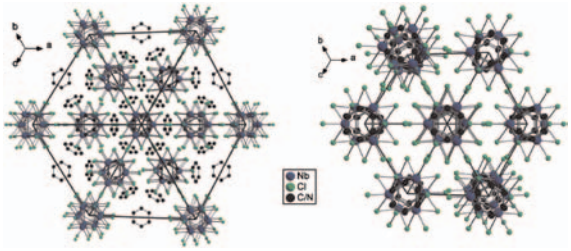

The synthesis and structure of a second cubic modification of $(PyrH)_2[Nb_6Cl_{18}]$ and of the new $(PyrH)_2[Nb_6Cl_{18}] \cdot EtOH$ are reported, both of which contain isolated niobium halide cluster anions with an octahedral core of metal atoms.

Continued

The transformation of ferrihydrite in the presence of trace Fe(II): The effect of the anionic media
Hui Liu, Hui Guo, Ping Li and Yu Wei
Page 2666

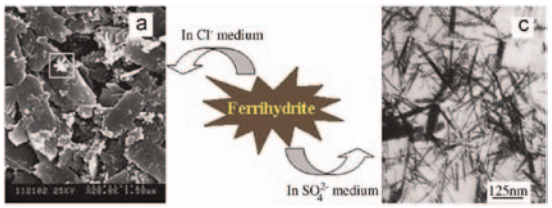

Fe(II)-induced transformation of ferrihydrite in sulfate-rich medium was studied. Lepidocrocite is a main ingredient in the product in Cl^- medium at room temperature (RT), while goethite is the only product in SO_4^{2-} medium. Goethite particles obtained in Cl^- medium are star-like but rod-like in SO_4^{2-} medium.

Hydrothermal synthesis and luminescent properties of $LuBO_3:Tb^{3+}$ microflowers
Jun Yang, Cuimiao Zhang, Lili Wang, Zhiyao Hou, Shanshan Huang, Hongzhou Lian and Jun Lin
Page 2672

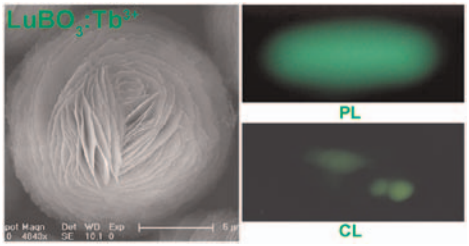

Hexagonal vaterite-type $LuBO_3:Tb^{3+}$ microflower-like phosphors have been successfully prepared by a simple and mild hydrothermal process directly. The reaction mechanism has been considered as the dissolution/precipitation mechanism; the self-assembly evolution process has been proposed on homocentric layer-by-layer growth style. The luminescent properties of the as-obtained $LuBO_3:Tb^{3+}$ samples have been investigated in detail, which shows it is a good green-emitting phosphor in fluorescent lamps and field emission displays potentially.

Surfactant-free synthesis of nickel nanoparticles in near-critical water
Peter Hald, Martin Bremholm, Steen Brummerstedt Iversen and Bo Brummerstedt Iversen
Page 2681

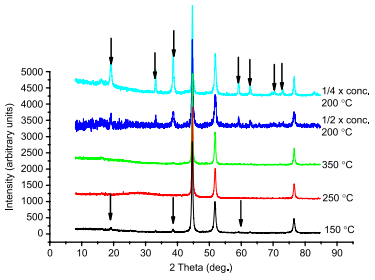

A surfactant-free synthesis route to nickel nanoparticles has been successfully transferred to near-critical water conditions reducing synthesis times from hours to seconds. Nickel nanoparticles in the 40–60 nm range have been synthesised from an ammonia stabilised hydrazine complex with the average size controlled by reaction temperature.

A density-functional study on the stability of anatase-type phases in the system Mg–Ta–O–N
Holger Wolff, Martin Lerch, Heikko Schilling, Carsten Bähtz and Richard Dronskowski
Page 2684

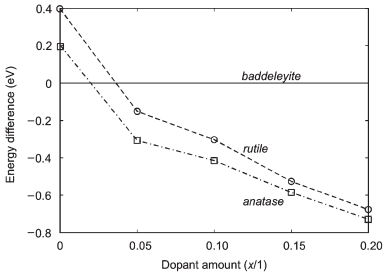

Density-functional total energy of Mg-doped TaON in several polymorphs, each in its most stable arrangement, as a function of the dopant amount.

Synthesis, structure and physical properties of the new Zintl phases $Eu_{11}Zn_6Sb_{12}$ and $Eu_{11}Cd_6Sb_{12}$
Bayrammurad Saparov, Svilen Bobev, Arif Ozbay and Edmund R. Nowak
Page 2690

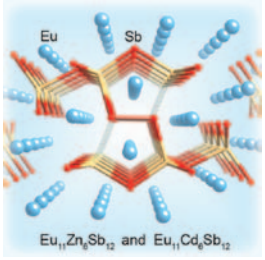

The synthesis, structure determination from single-crystal X-ray diffraction and magnetic properties of $Eu_{11}Zn_6Sb_{12}$ and $Eu_{11}Cd_6Sb_{12}$ are reported. Both compounds crystallize with the monoclinic space group $C2/m$, and their structure can be viewed as built of $ZnSb_4$ or $CdSb_4$ tetrahedra, which are connected through common corners and *exo*-bonds.

Impact of structural features on pigment properties of α-Fe_2O_3 haematite
N. Pailhé, A. Wattiaux, M. Gaudon and A. Demourgues
Page 2697

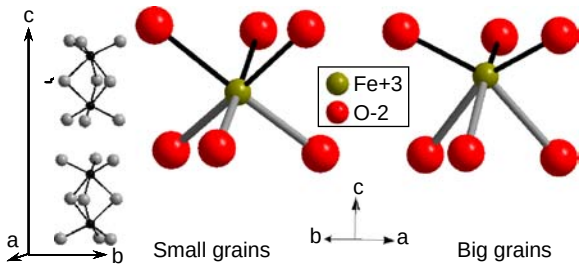

The reddish colour of Fe_2O_3 haematite was analysed in regard to its structural features, especially in regard to the Fe^{3+} octahedral site distortion, which is progressively less and less distorted from the centre towards the surface of the grains.

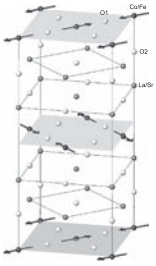

The reduced K_2NiF_4 phases $LaSrCo_{0.5}Fe_{0.5}O_{3.75}$ and $La_{1.2}Sr_{0.8}Co_{0.5}Fe_{0.5}O_{3.85}$ accommodate disordered oxide ion vacancies confined to equatorial planes of the structure. Magnetic exchange results in AFM order at low temperature, which can be represented by a tetragonal noncollinear model for the moments. Co^{3+} ions, present in stoichiometric $LaSrCo_{0.5}Fe_{0.5}O_4$ and $La_{1.2}Sr_{0.8}Co_{0.5}Fe_{0.5}O_4$, inhibit magnetic order and are assumed to be in the low-spin state.

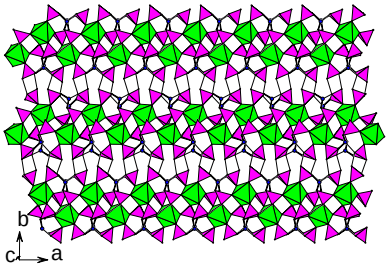

Two series of luminescent lanthanide phosphonates have been synthesized and structurally characterized. Their structures feature two different types of 2D sumpramolecular layers based on two types of 1D arrays interlinked via strong hydrogen bonds.

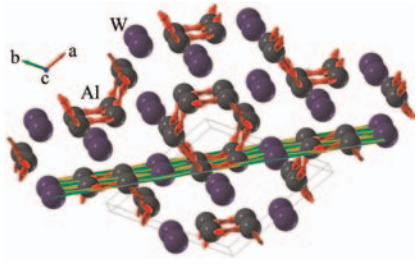

The novel compound WAl_2 is the first aluminide crystallizing with the $CrSi_2$ structure type. This compound is stable up to high pressures of at least 31.5 GPa. The chemical bonding analysis by means of the electron localization function (ELF) reveals a partially covalent bonding being responsible for the anisotropic compression behavior.

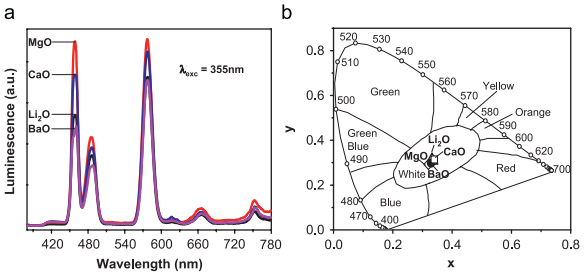

Tm^{3+} and Dy^{3+} ions co-doped aluminoborosilicate glasses, which emit white light under UV light excitation, were prepared. The dependence of luminescence properties on glass compositions was studied, and results showed that the white color luminescence was not affected significantly with different network modifier oxides. This adjustability could broaden application areas.

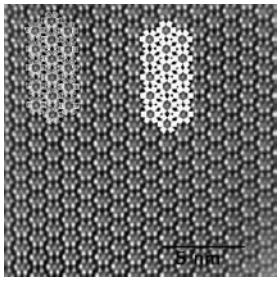

From the isopolyanion to the extended bulk tungsten oxide: HRTEM imaging.

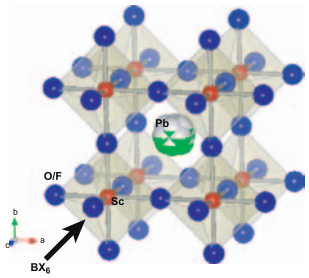

A novel perovskite-type oxyfluoride, $PbScO_2F$, was synthesized at high pressure (4 GPa) and temperature (1000 °C). This compound has a cubic perovskite-type structure in which the Pb ions are displaced along the ⟨110⟩ direction from the ideal *A*-site position.

Continued

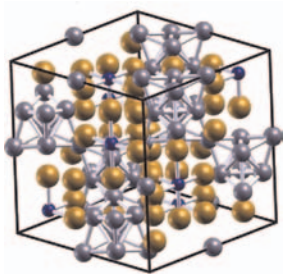

Ball and stick representation of the η-Ni_6Mo_6C crystal structure.

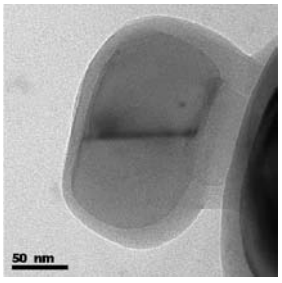

The article presents a simple sol–gel process through core–shell approach to the synthesis of low temperature sintered alumina–aluminium titanate. The lowering of the reaction temperature can be attributed to the maximisation of the contact surface between the reactant due to the core–shell approach. This material showed the better microstructure control compared to the standard solid-state mixing route.

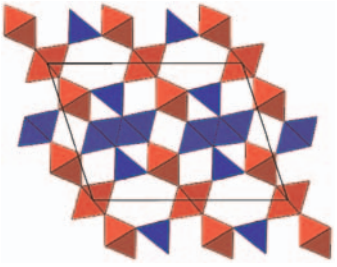

The structures of three beta-gallia–rutile intergrowths, expressed as $(Ga,In)_4(Sn,Ti)_{n-4}O_{2n-2}$, $n=6$, 7, and 9, were refined using Rietveld analysis of neutron time-of-flight powder diffraction data. The $n=6$ phase $Ga_{3.24}In_{0.76}Sn_{1.6}Ti_{0.4}O_{10}$ crystallizes in $P2/m$ whereas the $n=7$ and 9 phases crystallize in $C2/m$. All structure are similar in that they possess hexagonal tunnels parallel to the [010] vector.

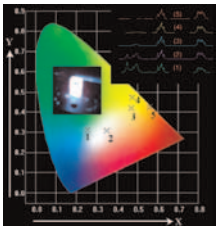

Under single 976 nm laser excitation, intense red, green and blue upconversion emissions were simultaneously observed owing to the successive energy transfer from Yb^{3+} to Ho^{3+} or Tm^{3+}. Various colors of luminescence, including bright perfect white light with CIE-$X=0.351$ and CIE-$Y=0.306$, can be easily tuned by adjusting the concentrations of the rare earth ions in the transparent oxyfluoride glass ceramics.

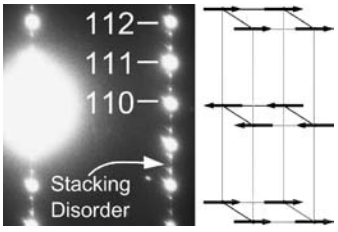

The anhydrous alums $KCr(SO_4)_2$, $RbCr(SO_4)_2$ and $KAl(SO_4)_2$ are characterized by X-ray and neutron powder diffraction and TEM diffraction. All compounds have octahedral coordination of the trivalent cations. Stacking disorder is observed, with the MO_6–SO_4 network of polyhedra rotated in opposite directions between layers. Low-temperature NPD reveals ferromagnetic in-plane ordering, with antiferromagnetic ordering between planes below 3 K.

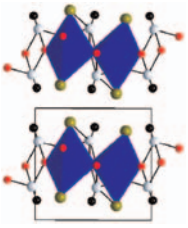

The synthesis, crystal structure determination, and magnetic properties of the new layered compound $CoSb_2O_3Br_2$ is reported. Structural Co–Co dimers are formed within the layers. The susceptibility below 25 K is typical for the onset of long-range antiferromagnetic correlations. Raman scattering and specific heat measurements both point to a structural instability leading to a loss of inversion symmetry below 6 K.

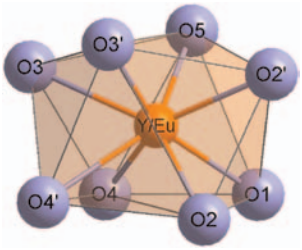

The unique rare-earth metal(III) site in $Y_2Te_4O_{11}$ coordinated by eight oxygen atoms in the shape of a distorted trigonal dodecahedron where also the Eu^{3+} cations of the doped compound reside.

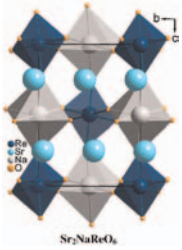

Single-crystal structure analyses of double perovskite rhenates, Sr_2LiReO_6, Ba_2LiReO_6 and Ba_2NaReO_6 indicate cubic symmetry while that of Sr_2NaReO_6 shows monoclinic symmetry.

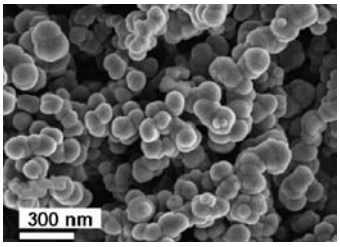

Carbon nanosheres with diameters between 100 and 400 nm have been succesfully synthesized via low-power laser assisted pyrolysis of anthracene in a nitrogen atmosphere. The developed facile route yields homogeneous nanoparticles and requires no supplementary carbon feedstock or catalyst. The sharp thermal gradient afforded by the laser results in two kinds of carbon products that differ in crystallinity and mean particle size. Our detailed findings point to the carbon nanospheres being comprised of nanosized unclosed aromatic layers that are connected together by simple organic linkers.

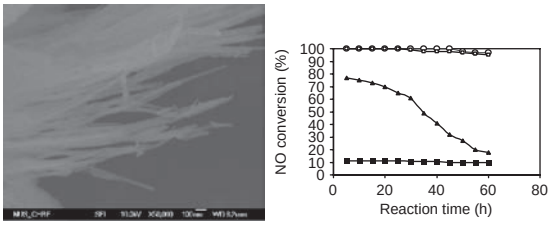

La_2CuO_4 nanofibers, made by use of single walled carbon nanotubes as templates under mild hydrothermal conditions, could catalytically decompose NO completely into nitrogen and oxygen at the low temperature of 300 °C.

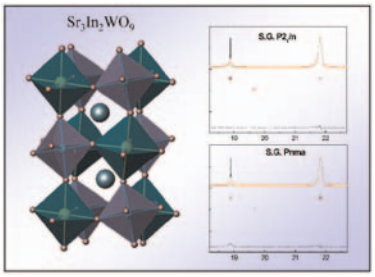

The structure of the new uranium-based double perovskite $Sr_3In_2UO_9$ is described and the true symmetry of the other title compounds are revisited. The presence of long-range ordering in the Sr samples, by contrast with the Ba perovskites, is related with the smaller unit cell and B–B distances in the Sr oxides, promoting the electrostatic repulsions between highly charged W^{6+} and U^{6+} cations as driving force for the long-range B-site ordering.

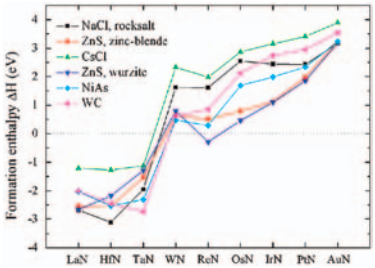

Formation enthalpy per formula unit ΔH (eV) for all the considered structures of 5*d* transition metal mononitrides MN (M = La–Au). It was shown that the formation enthalpy increases from LaN to AuN. The nitrides with negative values indicate that they can be synthesized experimentally at ambient conditions.

Continued

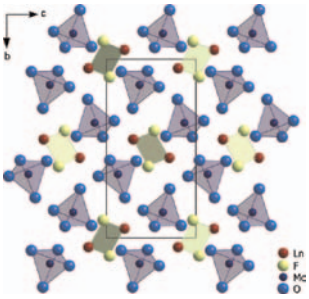

View at the crystal structure of *Ln*F[MoO_4] (*Ln* = Sm–Tm) along [100] with special emphasis on the isolated $[MoO_4]^{2-}$ tetrahedra (*blue*) and the $[F_2Ln_2]^{4+}$ rhombuses (*green*).

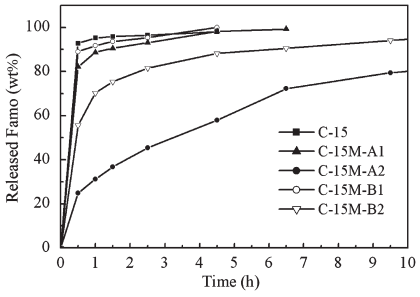

Trimethylsilyl-carboxyl bifunctionalized SBA-15 has been studied as carrier for controlled release of drug famotidine. To load drug with large capacity, SBA-15 with high content of carboxyl groups was successfully synthesized. After grafting trimethylsilyl groups on the surface of carboxyl functionalized SBA-15, the release of Famo was greatly delayed with the increasing content of TMS groups.

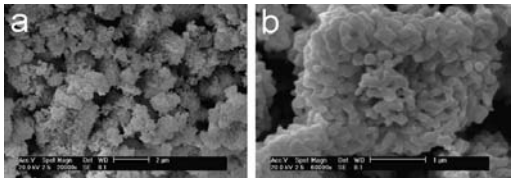

Excellent red phosphors gadolinium tungstate and molybdate with the formula $Gd_{(2-x)}MO_6:Eu_x^{3+}$ (*M* = Mo, W) were synthesized by the conventional solid-state reaction at 900 and 1300ºC for 4 h, respectively. SEM imagines indicate that the morphology of $Gd_{1.96}WO_6:Eu_{0.04}^{3+}$ has 3D micro-pore network structures better than the block-like $Gd_{1.96}MoO_6:Eu_{0.04}^{3+}$. Their quantum efficiency has been investigated.

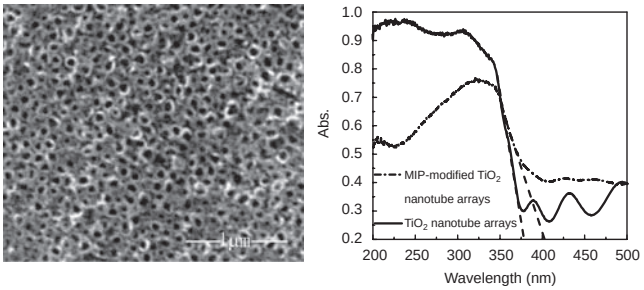

A tetracycline hydrochloride molecularly imprinted polymer modified TiO_2 nanotube array electrode was prepared via surface molecular imprinting. It showed improved response to simulated solar light and higher adsorption capability for tetracycline hydrochloride, thereby exhibiting increased PEC activity under simulated solar light irradiation. The apparent first-order rate constant was 1.2-fold of that on TiO_2 nanotube array electrode.

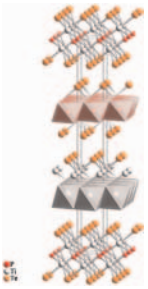

Crystal structure of Ti_2PTe_2 with stacking sequence of the hexagonal layers of anions and cations. Highlighted in red is the octahedral coordination of phosphorus by titanium, and in grey the octahedral coordination of titanium by phosphorus and tellurium.

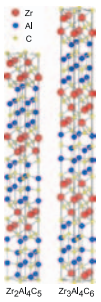

Crystal structures of new layered carbides $(ZrC)_2Al_4C_3$ and $(ZrC)_3Al_4C_3$.

Processing and characterization of new oxysulfide glasses in the Ge–Ga–As–S–O system

C. Maurel, L. Petit, M. Dussauze, E.I. Kamitsos, M. Couzi, T. Cardinal, A.C. Miller, H. Jain and K. Richardson

Page 2869

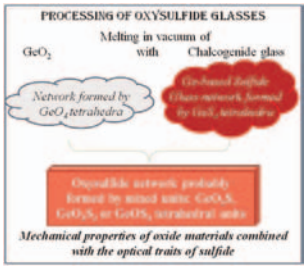

In this paper, we explain how new oxysulfide glasses are prepared in the Ge–Ga–As system employing a two-step process: (1) the processing of the chalcogenide glass (ChG) and (2) the re-melting of the ChG with GeO_2 powder. Raman, infrared and XPS spectroscopies show the formation of new oxysulfide structural units.

Quantum chemical study and low-temperature calorimetry of phase transition in $V_4S_9Br_4$

S.G. Kozlova, S.P. Gabuda, G.A. Berezovskii, D.P. Pischur, Y.V. Mironov, A. Simon and V.E. Fedorov

Page 2877

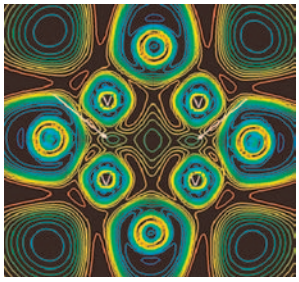

Dysinaptic basins of electron spin pairing in low-temperature phase $V_4S_9Br_4$ (arrows).

Author inquiries

Submissions

For detailed instructions on the preparation of electronic artwork, consult the journal home page at http://authors.elsevier.com.

Other inquiries

Visit the journal home page (http://authors.elsevier.com) for the facility to track accepted articles and set up e-mail alerts to inform you of when an article's status has changed. The journal home page also provides detailed artwork guidelines, copyright information, frequently asked questions and more.

Contact details for questions arising after acceptance of an article, especially those relating to proofs, are provided after registration of an article for publication.

Language Polishing

Authors who require information about language editing and copyediting services pre- and post-submission should visit http://www.elsevier.com/wps/find/authorshome.authors/languagepolishing or contact authorsupport@elsevier.com for more information. Please note Elsevier neither endorses nor takes responsibility for any products, goods, or services offered by outside vendors through our services or in any advertising. For more information please refer to our Terms & Conditions at http://www.elsevier.com/wps/find/termsconditions.cws_home/termsconditions.

For a full and complete Guide for Authors, please refer to *J. Solid State Chem.,* Vol. 180, Issue 1, pp. *bmi–bmv*. The instructions can also be found at http://www.elsevier.com/wps/find/journaldescription.cws_home/622898/authorinstructions.

Journal of Solid State Chemistry has no page charges.